Analysis of Sealing Performance and Mechanism of Biomimetic Superoleophobic Surface Structure

Q. Li, S. Cheng, Z. Hou†, W. Zhao, and Q. Guan

School of Mechanical and Vehicular Engineering, Changchun University, Changchun 130022, China

†*Corresponding Author Email: houzh@ccu.edu.cn*

ABSTRACT

Sealing performance is critical for mechanical components, particularly in automotive engines, where oil leaks remain a persistent challenge. This paper presents the design of novel biomimetic sealing surfaces that replicate the structural characteristics of biological surfaces with superhydrophobic and superoleophobic properties. A comprehensive evaluation of the design and performance of these biomimetic surfaces is provided. A multilayer microarray structure was designed using multivariate coupled mimetic theory. The structure consists of a smooth surface, a primary biomimetic weave surface, and a secondary biomimetic weave surface. Biomimetic superoleophobic surfaces of varying grades were fabricated on automobile engine gaskets through machining. This paper analyzes the dispersion of oil droplets, impact dynamics, and contact time between different surface structures using Volume of Fluid (VOF), Coupled Level Set and Liquid Volume (CLSVOF), and Computational Fluid Dynamics (CFD). The results demonstrate that the biomimetic textured surface significantly enhances oleophobicity by minimizing contact with oil droplets, reducing the maximum diffusion diameter by approximately 15% compared to a smooth surface. The interaction duration of oil droplets on the biomimetic surface is reduced by 14.7%, leading to improved sealing efficiency. This study indicates that finely structured biomimetic surfaces have promising applications in automotive sealing technology. Further miniaturization and optimization of these structures are expected to enhance sealing efficiency, particularly in demanding industrial environments.

1. INTRODUCTION

An effective sealing mechanism is crucial for the efficient operation of mechanical equipment (Zhang et al., 2020). In industries such as automotive, aerospace, and manufacturing, seal performance significantly impacts the safety, reliability, and service life of equipment (Farfán-Cabrera et al., 2018). However, conventional sealing surfaces often fail under extreme conditions and do not meet the demands of modern high-performance engineering (Dong et al., 2020; Zhang et al., 2021). As a result, the design of innovative sealing surfaces and related research has become a central focus in modern sealing technology (Wang et al., 2015).

The wetting behavior of rigid surfaces is crucial, particularly when these surfaces exhibit superhydrophobic effects with liquid contact angles greater than 150° (Jiang et al., 2018). This effect typically mimics the surface structures of certain organisms in nature, such as lotus leaves and crocodile skins, both of which display remarkable superhydrophobic properties. By studying these natural phenomena, new surface materials with enhanced hydrophobic and oleophobic properties can be designed to improve resistance to oil and moisture absorption (Barthlott et al., 2017; Jia et al., 2020). The micrometer and nanostructures of natural organisms, such as lotus and rice leaves, have been replicated in the design of biomimetic surfaces with superhydrophobicity. These advanced surfaces utilize microscopic voids to create an air cushion, reducing direct fluid-surface interaction and adhesion. The Air Cushion Effect is defined as the formation of a thin layer of air between a drop of liquid (such as oil or water) and a texture or microtexture. This air layer acts as a physical barrier, hindering the liquid's direct contact with the solid surface, significantly reducing adhesion and altering droplet wetting behavior (Luo et al., 2018). Integrating this technology into mechanical systems, particularly sealing components, significantly reduces the dynamic friction during continuous motion,

thereby decreasing the associated heat generation and energy loss. By lowering the total surface energy requirement, minimizing the interaction area between the fluid and the surface further contributes to improved energy efficiency (Feng et al., 2008; Gose et al., 2018). Incorporating biomimetic superhydrophobic properties into sealing surfaces is expected to enhance sealing efficiency and extend service life.

Researchers have analyzed the microstructure of various natural organisms, including certain plants and animal skins. These insights have contributed to the development of biomimetic superhydrophobic surfaces, which are self-cleaning, anti-icing, corrosion-resistant, and multifunctional, with applications in oil-water separation and other areas (Wang et al., 2013). The superhydrophobic and self-cleaning properties of the lotus leaf have attracted considerable attention from the scientific community. Liang et al. investigated the micro-nanostructures present on lotus leaf surfaces. These structures isolate air, reducing the contact area between the micronanometer structures and the liquid drop. The researchers modeled the lotus leaf's superhydrophobicity and self-cleaning properties by lowering its surface adhesion (Liang et al., 2016). Ding et al. (2019) improved surface properties by designing various conical-shaped structures, significantly enhancing their superhydrophobic properties and static contact angle, which increased from approximately 107° to over 172°. Recent studies have examined the mechanical properties of liquid drops impacting biomimetic superhydrophobic surfaces. The dynamics of surface droplet impact behavior include several key processes, such as droplet spreading, deposition, instantaneous splashing, retraction fragmentation, and secondary rebound (Marengo et al., 2011; Gao et al., 2021). Superhydrophobic surface structures have been shown to significantly influence the physical properties of droplets (Wu et al., 2011). Lin et al. (2020) studied the interaction time between two similar drops on different textured surfaces and found that, compared to a smooth biomimetic superhydrophobic surface, a coarse surface significantly reduced the contact duration. Gauthier et al. examined the effect of drop velocity and surface structure on interaction time. Their findings indicated that the interaction duration decreases with increasing impact velocity. They also observed that varying the shape of the weave resulted in shorter interaction times on pitted surfaces compared to flat surfaces (Gauthier et al., 2015). Vander Veen et al. (2014) proposed that, in addition to droplet inertia, the air-gap size also influences the height of the gas membrane under the droplet. On structured superhydrophobic surfaces, this air film enables droplets to rebound completely. In contrast, on other surfaces, droplets may adhere completely or rebound only partially, with some droplets still sticking. Altering the droplet contact area by modifying surface properties can enhance sealing performance (Gao et al., 2021; Wang et al., 2015).

Advances in CFD have enabled researchers to study droplet impact behavior on specific wettable surfaces (Serevina & Meyputri, 2015). The droplet impact process involves two-phase flow and requires accurate interfacial tracking. Common methods used include Eulerian and Lagrangian models. Eulerian models typically employ Volume of Fluid (VOF) and Level Set methods to accurately track the interface (Nagashima & Sawada, 2016; Wu et al., 2018). Liu et al. applied CFD and VOF models to trace the gas-liquid-solid interface on superhydrophobic surfaces, illustrating the dynamics of the interface during droplet impact (Liu et al., 2020).

Biomimetic surfaces inspired by the phenomenon of natural superhydrophobicity have recently attracted significant attention due to their unique wetting properties. While many studies have explored sealing applications on these surfaces, detailed analysis of fluid interface behavior on complex microstructured surfaces remains limited. This paper systematically investigates droplet dynamics on a newly designed multilayer biomimetic microarray surface using advanced CFD techniques. The main contribution of this study is the detailed analysis of fluid interface behavior using VOF and Level Set models. These models were used to accurately track the gas-liquid-solid interface, providing new insights into the dynamic diffusion, retraction, and rebound of oil droplets on both primary and secondary biomimetic structures. Inspired by the micrometer and nanostructures of naturally superhydrophobic surfaces, these designs aim to minimize fluid contact with the surface, thereby enhancing sealing effectiveness.

2. MATERIALS AND METHODS

2.1 Materials

In natural phenomena, dogwood leaves exhibit excellent superhydrophobic properties and anisotropic surfaces. Figure 1(a-d) shows SEM images of the dogwood leaf surface at magnifications of 50X, 40X, and 200X, respectively. As shown in Fig. 1(b) and (c), the surface of the dogwood leaf blade features a microarray structure composed of parallel millimeter-sized grooves aligned with the main leaf veins. The width, depth, and
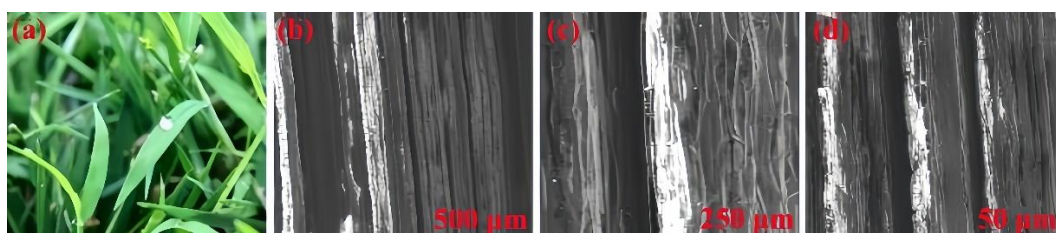
Fig. 1 Microarray structure on the surface of dogwood leaves

(a)   (b)
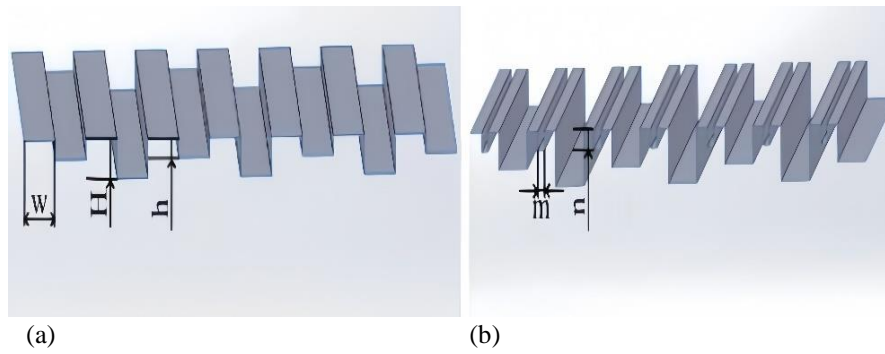
Fig. 2 Different microtextured surfaces: (a) primary bionic microtextured surface, (b) secondary bionic microtextured surface

gap between each groove are relatively uniform. The enlarged view of the regular groove structure in Fig. 1(d) reveals small submicrometer striations on the trench surface, with an average dimension ranging from 2 μm to 5 μm. Dogwood leaves possess regular sub-millimeter composite grooves that minimize the interfacial area for droplet-surface interactions. Moreover, the air trapped within the grooves reduces the viscosity of the droplet surface, facilitating its movement toward the chip and resulting in a secondary rebound phenomenon.

In this study, asbestos and rubber composites are utilized as the base material for automotive engine block gaskets. Their excellent adaptability and corrosion resistance make them suitable for high-temperature and high-pressure engine environments (Dodson & Hammar, 2005). Additionally, their low cost facilitates mass production.

Numerical simulations were conducted using ANSYS Fluent 21R1 within a rectangular computational domain measuring 10 mm × 10 mm × 20 mm. The lower boundary consisted of three different surfaces: one smooth asbestos sheet and two based on the microstructural design of dogwood leaves. These surfaces were modeled as a one-stage microarray with a multilevel groove composite structure. Surface models were created in SOLIDWORKS, defining microstructures to represent smooth surfaces, primary bionic weave structures, and secondary bionic weave structures. The microgroove width is denoted as w, the small groove width as h, and the large groove width as H, as shown in Fig. 2(a). A smaller braided unit was added to the main braided layer, resulting in a secondary microarray model with a trench width of m and a height of n, as shown in Fig. 2(b).

The biomimetic microweave surface incorporates bio-inspired, numerically optimized microstructures modeled after dogwood leaves. This woven surface design combines bio-inspired structures with optimized microstructures based on the dogwood leaf blade, which reduce the contact area of water droplets and create an air cushion effect. In this study, the primary microgroove size, similar to that of dogwood blades, was selected to facilitate air capture during oil droplet impact. Additionally, CFD simulations were conducted to adjust and optimize the geometric parameters of the micro-textured structure, determining the optimal size for the secondary microstructure. This multilayer composite structure minimizes the oil droplet contact area, enhancing oil resistance and sealing efficiency.

For the preparation of engine block gasket surface samples, asbestos and rubber composites were selected as substrate materials to ensure stability and reliability under the experimental conditions. Initially, a smooth sealing surface was created using a traditional polishing process. Subsequently, inspired by the microstructure of dogwood leaves, a first-order bionic braided structure was fabricated on the spacer using laser processing. Finally, a secondary bionic weave surface was created by adding micrometer-scale structures to the primary bionic weave surface. Conventional smooth washers were analyzed as a baseline for comparison.

2.2 Methods

2.2.1 Fluent Numerical Simulation Method

Numerical simulations employed the CLSVOF method to track the oil droplet interface. To effectively capture the highly deformed structure of the simulated oil droplets during spreading, the CLSVOF technique was implemented (Walters & Wolgemuth, 2009). This method combines a VOF approach for volume and mass conservation with a level set method for precise interface tracking (Talebanfard et al., 2019). With this VOF scheme, the volume fractions of different fluid phases and their interacting interfaces are monitored throughout the entire domain. This approach allows for accurate prediction of droplet spreading, contraction, and rebound behavior (Nekouei & Vanapalli, 2017; Baggio & Weigand, 2019). The volume fraction discretization equation (1) used in the VOF method is:

$$\frac{\vartheta_q^{t+1}\rho_q^{t+1} - \vartheta_q^t\rho_q^t}{\Delta t}V + \sum_f \left(\rho_q^{t+1}U_f^{t+1}\vartheta_{qf}^{t+1}\right) = \left[s_{\vartheta_q} + \sum_{p=1}^n\left(\overset{\&}{m}_{pq} - \overset{\&}{m}_{qp}\right)\right]V \quad (1)$$

In equation (1), ϑ_{qf}^{t+1} represents the volume fraction of phase q, U_f^{t+1} is the volume flux across the surface, s_{ϑ_q} indicates the source term, $\overset{\&}{m}$ denotes mass exchanged between phases, V and ρ stand for unit volume and density, respectively, $t+1$ is the time-step exponent, and n is the total phase count. The volume fraction must comply with equation (2):

$$\sum_{q=1}^n \vartheta_q = 1 \quad (2)$$

The energy conservation equations (3-6) ensure the conservation of energy across the solid-liquid-gas phases and are implemented using the Fluent method.

$$\frac{\partial}{\partial t}(\rho E)+\nabla\cdot(\vec{v}(\rho E+p))=\nabla\cdot\left[k_{eff}\nabla T-\sum_q\sum_j h_{j,q}\vec{J}_{j,q}+(\bar{\bar{\tau}}_{eff}\cdot\vec{v})\right]+S_h$$

$$(3)$$

$$E=\frac{\sum_{q=1}^{n}\vartheta_q\rho_q E_q}{\sum_{q=1}^{n}\vartheta_q\rho_q}$$

$$(4)$$

$$E_q=h_q-\frac{p}{\rho_q}+\frac{v^2}{2}$$

$$(5)$$

$$\vec{J}_j=-\left(\rho D_{j,m}+\frac{u_t}{s_{c_t}}\right)\nabla Y_j-D_{T,j}\frac{\nabla T}{T}$$

$$(6)$$

The Level Set (LS) method is a numerical simulation technique used to model the dynamic interaction in fluid dynamics. It employs a scalar function ϕ to represent the signed distance from any point to the interface. A positive or negative value indicates the position relative to the boundary, with 0 defining the interface itself. This distance is determined by the relative position to the boundary, which always lies on the surface ψ. The expression for the scalar function is given in Equation (7):

$$\phi(x,y,z)=\begin{cases}|d| & for(x,y,z)\,in\quad liquid\\ 0 & for(x,y,z)\in\psi\\ -|d| & for(x,y,z)\,in\quad gas\end{cases}$$

$$(7)$$

In expression (7), a variable $|d|$ is the distance between a selected point and an interface. When the selected point is in the liquid phase, constant ϕ is positive, but it will be negative if it is in the gaseous phase.

The dynamic properties of interfaces are crucial in the study of Level Set (LS) methods, particularly in simulating multiphase flow regimes. In these systems, the interactions between various elements, such as droplets, bubbles, and liquid films, are primarily influenced by interfacial tension. In the LS method, surface tension effects are typically represented by a continuous equation, which is used to calculate interface curvature and the normal orientation of the interface. In the Continuous Surface Force (CSF) model, the momentum conservation equation is modified by adding a source term to account for the effect of surface forces (Zhang et al., 2020). Consequently, the expression for continuous surface tension (8) is derived using the discretization theorem:

$$\begin{cases}F_{CSF}=\sigma\gamma\nabla\vartheta_2\dfrac{\rho_1\vartheta_1+\rho_2\vartheta_2}{1/2(\rho_1+\rho_2)}\\[2mm] n=\dfrac{\nabla\vartheta_2}{|\nabla\vartheta_2|}\\[2mm] \gamma=-(\nabla\cdot n)=\dfrac{1}{|n|}\left[\left(\dfrac{n}{|n|}\cdot\nabla\right)|n|-(\nabla\cdot n)\right]\end{cases}$$

$$(8)$$

In expression (8), σ represents the surface tension coefficient, γ denotes the surface curvature, n is the surface normal vector, and ϑ is the volume fraction of each phase, where indices 1 and 2 indicate the gas and liquid phases accordingly.

On rigid surfaces, the static contact angle is often applied as a parameter to adjust the shape of the gas-liquid boundary, while wall adhesion is also considered (Li et al., 2022). The cell vector n of the wall cell boundary perpendicular to the interface is given by formula (9):

$$n=n_s\cos\theta_w+\tau_s\sin\theta_w$$

$$(9)$$

τ_s in Eq. (9) is the tangential unit vector of the wall and n_s is the normal unit vector.

Wetting phenomena at solid-liquid interfaces can be explained in terms of interfacial energy, which provides an energy-based perspective on surface wettability (Wang et al., 2021). As shown in Fig. 3, when a liquid (L) is in contact with a solid (S), the atoms or molecules on the surface of the liquid and the solid are more energetic than the atoms or molecules inside them, and this extra energy can be expressed as surface tension or as a surface energy γ. The work of adhesion (W_{SL}) is expressed as:

$$W_{SL}=\gamma_{SA}+\gamma_{LA}-\gamma_{SL}$$

$$(10)$$

In equation (10), γ_{SA} is the surface energy at the solid-air interface, γ_{LA} is the surface energy at the liquid-air interface and γ_{SL} is the interfacial energy between the solid and the liquid.

As drops are deposited on a surface, the drops are maintained in their form, and their contact angles are equal to that of balance (for example, in Fig. 3). The contact angle θ can be determined by Young's equation with the Young's equation expression (11):

$$\gamma_{SL}=\gamma_{SA}-\gamma_{LA}\cos\theta$$

$$(11)$$

2.2.2 Energy Conversion Analysis

The overall energy E_{t0} of the oil droplet at its initial condition includes gravitational potential E_{p0}, surface tension energy E_{s0}, and kinetic energy E_{k0}. The internal temperature of the drop is supposed to be even, so it is neglected to consider the internal temperature variation. Its initial kinetic energy expression (12) is:

$$E_{t0}=E_{p0}+E_{s0}+E_{k0}$$

$$(12)$$
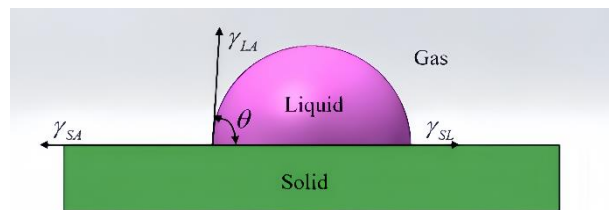
Fig. 3 Conservation of energy in the equilibrium state of contact between a droplet and a solid

The simulation of a given oil drop with the following initial characteristics was conducted: diameter D_0, mass m, density ρ, and gas-liquid surface tension $\sigma_{\lg}$. The individual components of the initial energy can be expressed in terms of the quantities given above as (13-16) (Huang et al., 2016):

$$E_{p0} = mgh_0 \tag{13}$$

$$E_{s0} = \sigma_{\lg}\pi D_0^2 \tag{14}$$

$$E_{k0} = 0.5\rho\left(\frac{1}{6}\pi D_0^3\right)v_0^2 \tag{15}$$

$$m = \rho\left(\frac{1}{6}\pi D_0^3\right) \tag{16}$$

The energy conversion equation (17-19) is derived as follows (Yarin., 2006):

$$E_t = E_p + E_s + E_k \tag{17}$$

$$E_s = \sigma_{\lg}S_{\lg} + 0.25\sigma_{sl}S_{sl} - 0.25\sigma_{sg}S_{sg} \tag{18}$$

$$\sigma_{sl} = 0.5\sigma_{\lg}\left(\sqrt{1+\sin^2\theta} - \cos\theta_w\right) \tag{19}$$

Here, S represents the contact area of each item, lg represents liquid-gas, sl represents solid-liquid, and sg represents solid-gas.

In numerical modeling, directly obtaining the kinetic energy of oil droplet impacts presents a challenge. To precisely calculate the kinetic energy of an oil droplet in a multiphase flow, we employ a mathematical limit approach that partitions the droplet's interior into N equal sections. Then, the kinetic energy of the drop can be represented by (20):

$$E_k = \sum_{i=1}^{N} 0.5\frac{m}{N}v_i^2 = 0.5m\left(\frac{1}{N}\sum_{i=1}^{N}v_i^2\right) = 0.5mv_{mean}^2 \tag{20}$$

Oil droplets impacting a surface are accompanied by an energy loss, the energy loss expression (21) (Li et al., 2022) is shown below:

$$E_d = \left(E_{p0} + E_{s0} + E_{k0}\right) - \left(E_p + E_s + E_k\right) \tag{21}$$

In order to evaluate the energy conversion rate, Li and Yang et al. conducted a comprehensive study of the droplet impact process under specific conditions. The data led to these conclusions: at first contact between the liquid and solid, E_t, E_P, and E_k exhibited a notable decrease; subsequently, with the diffusion of the droplet, E_s exhibited a decline and subsequent increase; The conversion of E_s to E_k happens during droplet retraction, while the rebound afterward increases E_s due to liquid elongation.

2.2.3 Fluent Numerical Calculation Settings

Surface wetting is a critical property that governs a fluid's diffusion on a solid surface, characterized by the contact angle and contact hysteresis (Li et al., 2021). This study examines the variation in dispersion conditions and the interaction time of the droplet. Due to the hydrophilic nature of smooth surfaces, the contact angle is treated as a fixed value to simplify the simulation calculations. In the boundary setup, the wall adhesion effect (contact angle) at the solid-liquid interface is defined to capture interactions between oil droplets and surface textures. The contact angle setting influences the curvature and behavior of the gas-liquid interface, playing a key role in realistic droplet impact dynamics. The contact angle is set to 70° for smooth surfaces and 153° for bionic superhydrophobic surfaces (Guo & Liu, 2007). These values correspond to hydrophilic (smooth) and superhydrophobic (textured) surfaces, respectively, and are consistent with the properties of natural surfaces such as dogwood leaves. The chosen contact angle simulates dynamic behaviors such as droplet spreading, retraction, and potential secondary rebound on the bionic surface. These considerations contribute to the accurate modeling of interfacial dynamics, such as oil droplet deformation and detachment. This approach facilitates the study of impact-related behaviors on different textured surfaces and helps explain variations in sealing performance.

To simplify the simulation, Fluent excludes heat transfer and phase change models when calculating the effect of droplets on smooth and superhydrophobic surfaces.

Figure 4 illustrates the computational domain representing the experimental setup for oil droplet impacts on solid surfaces. An oil droplet with a computational domain size of $10 \times 10 \times 20$ mm³ and a diameter of D_0 is released from a height under the influence of gravity (g = 9.81 m/s²), providing the droplet with an initial velocity v_0 upon impact. The bottom edge of the computational domain is modeled with a no-slip boundary condition, while the remaining surfaces are assigned an outlet boundary condition with a value of 0. The computational domain is discretized using the Cartesian method with a mesh size of 0.1 mm, resulting in a total of 2,798,096 mesh elements. The SIMPLEC algorithm is employed in Fluent for pressure-velocity coupling to enhance computational accuracy. Pressure difference values are computed using the PRESTO scheme, the volume fraction is solved using the Geo-Reconstruct method, and other spatially discrete variables are calculated using the second-order upwind scheme. The oil droplet density is set to 843 kg/m³, the viscosity is 0.0757 Pa·s, and the calculation process spans 1000 time steps, each lasting 0.00005 s.

Using Fluent, the diffusive diameter and interaction time of the droplet were calculated to assess its effect on the solid surface. The maximum diffusion diameter ($D-\max$) and interaction duration (t_c) characterize the behavior of oil droplets on different surfaces, allowing for comparison of the contact areas.

2.2.4 Mesh and Experimental model validation

Mesh independence verification is essential for
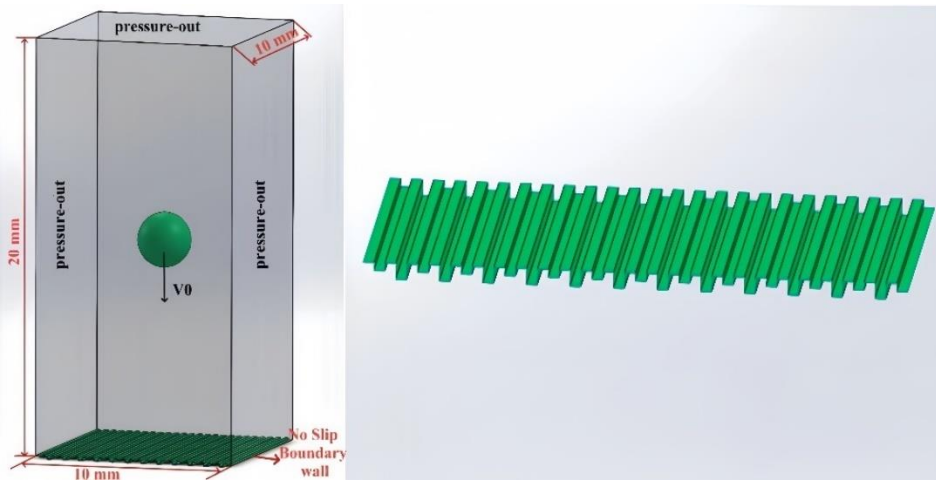
Fig. 4 Physical modeling of oil droplet impacts on computational domain surfaces
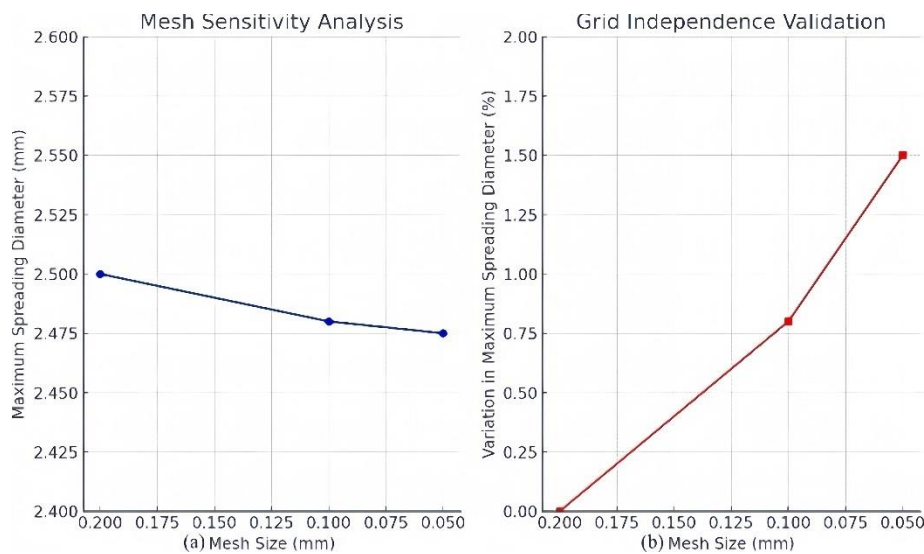
Fig. 5 (a) Mesh Sensitivity Analysis, (b) Grid Independence Verification

ensuring the accuracy and reliability of CFD simulation results, as it confirms the convergence of results before formal simulations are conducted (Li et al., 2022). The rate of change, $R(n)$, of D/D_0 is derived from the dimensionless spreading diameter, determined by adjacent grids, and is defined by equation (22) as follows:

$$R(n) = \left| \frac{(D/D_0)_n - (D/D_0)_{n+1}}{(D/D_0)_n} \right| \times 100\% \qquad (22)$$

Eq. (22) represents the dimensionless spreading diameter for the current grid count and $(D/D_0)_{n+1}$ denotes the dimensionless spreading diameter for the subsequent grid count. In this case, if the predicted dimensionless spreading diameter shows only minor variation with the number of grids, the mass and density of the grids are considered to meet the calculation requirements.

Figure 5(a-b) illustrates the mesh sensitivity analysis and mesh independence validation. Figure 5(a) shows the relationship between mesh size and the maximum diffusion diameter of the oil droplet. The diffusion diameter decreases slightly with grid refinement

(decreasing grid size). When the grid size is reduced below 0.1 mm, little further change is observed, indicating result stability and supporting the choice of 0.1 mm as the optimal grid size. Figure 5(b) presents the grid independence validation, displaying the percentage change in maximum spreading diameter for different grid sizes. When the grid size is reduced to below 0.1 mm, the variation remains below 2%, demonstrating that further mesh refinement has minimal impact on the results (Chila Kaminski, 2008). This confirms that the selected mesh size of 0.1 mm is sufficient to accurately capture the interface dynamics in the CLSVOF simulations.

This study developed an experimental platform to investigate oil droplet impact on surfaces, observing interfacial spreading and changes in droplet morphology, as shown in Fig. 6. The platform consists of a high-speed video camera, a lighting system, an injection device, a test sample, and an optical experimental base. The high-speed video camera captures transient images of the impact on the sample surface and, through signal transfer and image post-processing, generates high-frame-rate videos of the oil droplet motion.
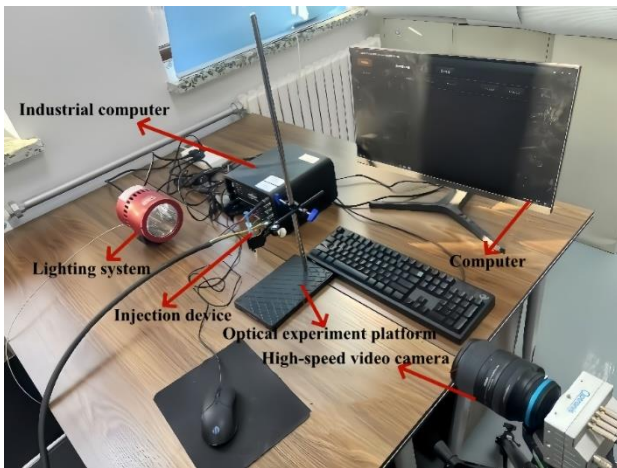
Fig. 6 Surface/Interface Oil Droplet Impact Test Process Experimental Platform
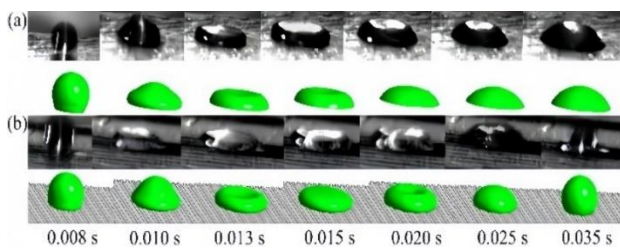
Fig. 7 Validation analysis of the effect of oil droplets on different structured surfaces: (a) Smooth sample surface, (b) Bionic microarray sample surface

The evolution of droplet morphology on uniformly distributed microstructures is independent of the initial impact location, indicating that the impact center does not influence the diffusion behavior (Liu et al., 2020). Oil droplets with a diameter of $D_0 = 2.6$ mm impact a surface with a bionic structure at a velocity of 0.5 m/s. To validate the accuracy of the Fluent numerical simulation method for modeling oil droplet impact dynamics on non-smooth oleophobic surfaces, experimental data and simulations of oil impacts on smooth and microarray superoleophobic surfaces were analyzed and compared. The analysis involved releasing the oil droplet at different impact locations. The results are shown in Fig. 7, where Fig. 7(a) illustrates the impact diffusion state at various moments after the oil droplet hits the smooth surface, recorded by a high-speed camera and compared to numerical simulations. Figure 7(b) shows the impact diffusion states at different moments after the oil droplets hit the microarray surface, captured by a high-speed camera and compared with numerical simulation results. Comparison of experimental and numerical results demonstrates strong consistency in the kinetic behavior and diffusion patterns of oil droplets on the biomimetic surface. The spreading diameter of the oil droplet increases sharply and then decreases rapidly, reaching the maximum spreading state at 0.015 s. At 0.035 s, the oil droplets on the biomimetic structure begin to exhibit a tendency to detach. These findings confirm that the numerical simulation method, coupled with the CLSVOF model for interfacial mechanics, can accurately model the morphological

changes of oil droplets on non-smooth surfaces and capture the flow behavior at solid-liquid-gas multiphase interfaces. Therefore, this computational method can be used to further explore the mechanical interaction between oil droplets and non-smooth bionic superoleophobic surfaces.

3. RESULTS AND DISCUSSION

3.1 Analysis of Oil Droplet Impact Behavior on Different Structured Surfaces

The kinetic behavior of droplets impacting a surface serves as a key reference for analyzing the mechanical behavior of biomimetic superhydrophobic surfaces at the interfacial level (Yarin et al., 2006). However, the impact behavior of droplets is primarily influenced by several key parameters, including surface tension, viscosity, and density. Surface characteristics, such as microarray structure, surface energy, and chemical composition, significantly affect droplet impact behavior. Therefore, in this study, numerical simulations were employed to analyze the impact of oil droplets on bionic surfaces subjected to different processing techniques. The goal was to investigate the influence of microarray structure variability on oil droplet spreading behavior.

The variation in the spreading coefficient (ε) and anisotropic spreading ratio (κ) over time is analyzed to investigate the dynamic behavior of oil droplets on the bionic surface. The validated Fluent numerical simulation method was employed to quantitatively compare and analyze the spreading diameters of oil droplets on surfaces with parallel and perpendicular groove structures across three different surface configurations. This analysis aimed to assess the differences in the dynamic behavior of oil droplets under varying impact velocities. The impact velocities considered in the study were as follows: v_O =0.5 m/s, v_O =1.0 m/s, v_O =1.5 m/s and v_O =2.0 m/s. By selecting these velocities, the effects of different kinetic energies on oil droplet behavior, particularly in terms of diffusion, retraction, and potential rebound, were systematically examined. Lower velocities were chosen to study initial spreading and adhesion phenomena, which are crucial for evaluating surface wetting behavior and static interaction properties. In contrast, higher velocities allowed for the investigation of the oil droplet's dynamic response, including secondary rebound and energy dissipation, which are important for assessing overall seal performance.

In the low-velocity impact region, defined by We values between 0.2 and 100, two primary outcomes can be observed: deposition and rebound (Zhao et al., 2021). Within a wider wettability range ($73° \leq \theta < 100°$), viscous forces between the droplet and surface become more significant. This increases viscous dissipation, reducing the droplet's initial energy, which may lead to deposition on the surface. Conversely, at a contact angle of $100° \leq \theta \leq 162°$ with low wettability, viscous forces between the droplet and surface are minimal, resulting in low viscous dissipation during impact. This allows the
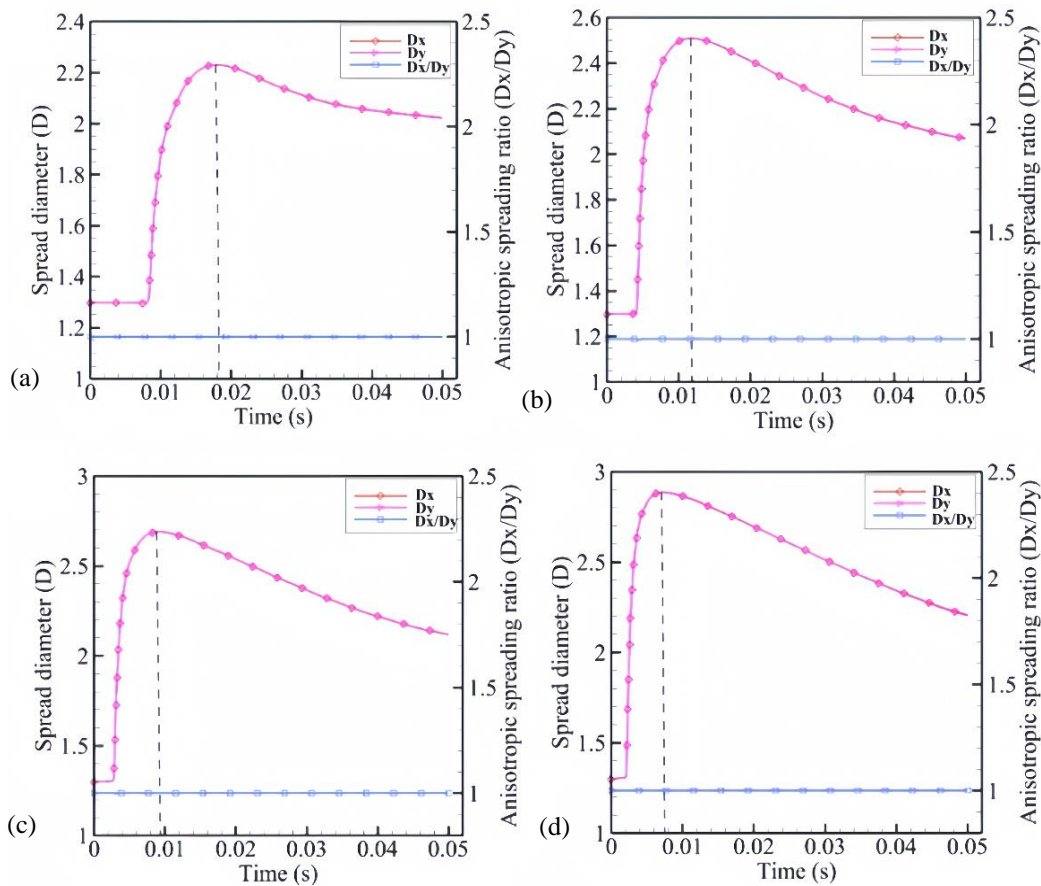
Fig. 8 Time-Varying Curves of Spreading Diameter and Anisotropic Spreading Ratio of Oil Droplets on Smooth Surfaces with Different Impact Velocities: (a) v_0 =0.5 m/s, (b) v_0 =1.0 m/s, (c) v_0 =1.5 m/s, (d) v_0 =2.0 m/s

droplet to rebound with sufficient energy after retraction (Huang et al., 2016), occurring when its kinetic energy exceeds the combined surface energy and the minimum gravitational potential energy at the end of spreading and retraction.

3.1.1 Analysis of Oil Droplet Impact Behavior on Smooth Surfaces

The variation in the diffusion radius and anisotropy distribution rate of the droplet on the smooth structure is shown in Fig. 8 (a-d). When oil droplets impacted the surface at a lower velocity (0.5 m/s), as shown in Fig. 8(a), they initially spread rapidly, reaching a maximum diameter of 2.23 mm at 0.017 s. Subsequently, the oil droplets gradually reduced in size and ultimately adhered to the smooth surface. Due to the uniform anisotropic properties of the smooth surface, the diffusion rate remained constant at 1 in both the X- and Y-directions. As the smooth surface exhibits equal anisotropic properties in all directions, the propagation rate is constant at 1 in both the X- and Y-directions. Figure 8(a-d) demonstrates that as the oil droplet's impact velocity (v_0) increases, the time to reach the maximum spreading diameter decreases, while the diameter itself increases. At an impact velocity of 2.0 m/s, the maximum spreading diameter of the oil droplet reaches 2.89 mm, with a time of only 0.007 s to reach this diameter.

As the impact velocity (v_0) increases, the oil droplets acquire greater initial kinetic energy, leading to a faster expansion process immediately following impact. The higher kinetic energy enables the droplets to quickly overcome surface resistance, thereby accelerating the spreading rate. Consequently, the time required for the droplets to reach their maximum spreading diameter decreases. As the impact velocity continues to rise, the increased kinetic energy allows the droplets to spread further before retracting. In the absence of structural barriers on smooth surfaces, oil droplets can achieve larger diffusion diameters, as there are no microstructures to limit droplet diffusion or induce additional retraction forces. Therefore, at an impact velocity of 2.0 m/s, the maximum spreading diameter of the oil droplet reaches 2.89 mm.

3.1.2 Analysis of oil Droplet Impact Behavior on Bionic Microtextured Surfaces

Figure 9 (a-d) shows the time-dependent curves of diffusion diameter and diffusivity for oil droplets impinging on the primary bionic microtextured surface at different velocities. Figure 9(a) illustrates that the oil droplets spread rapidly, reaching maximum diameters of 2.03 mm in the D_x-direction and 1.98 mm in the D_y-direction at 0.0127 s. Subsequently, the oil droplets underwent a process of shrinkage, ultimately resulting in a secondary rebound away from the surface of the primary
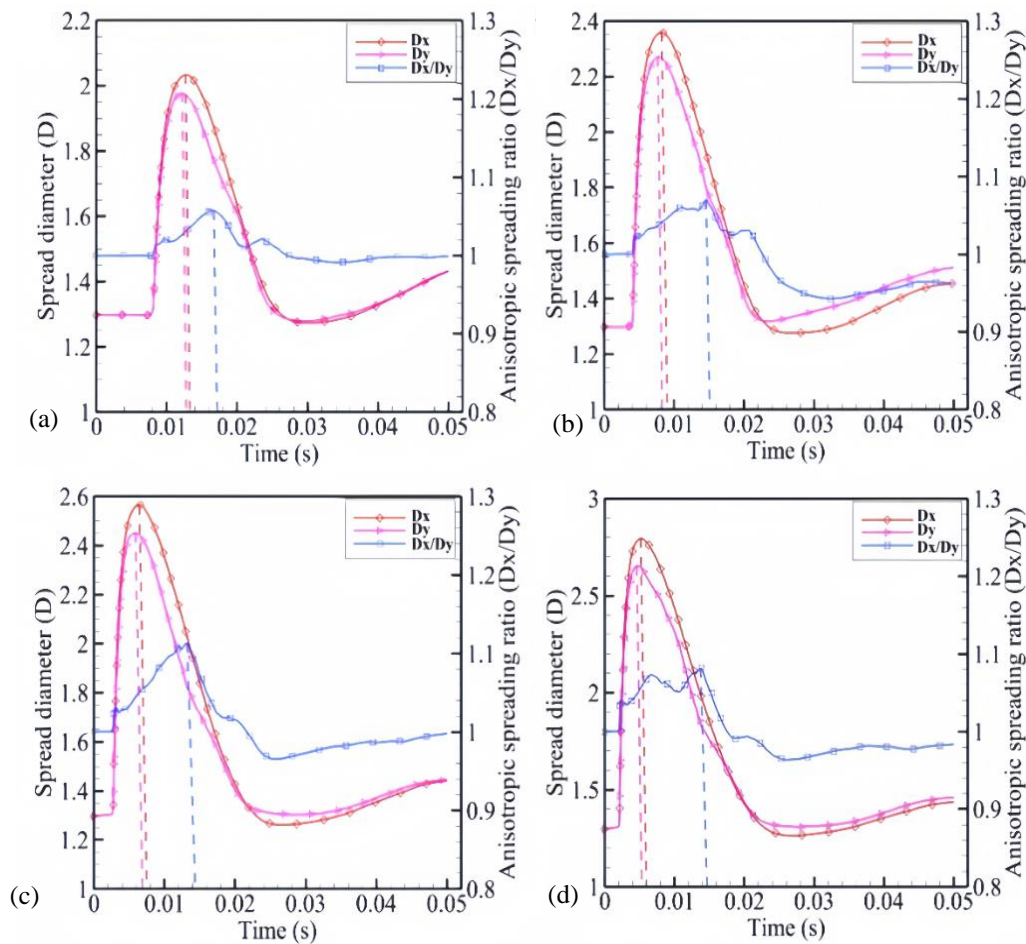
Fig. 9 Time-Varying Curves (of Spreading Diameter and Anisotropic Spreading Ratio of Oil Droplets on Ordinary Bionic Surfaces for Different Impact Velocities: (a) v_0 =0.5 m/s, (b) v_0 =1.0 m/s, (c) v_0 =1.5 m/s, (d) v_0 =2.0 m/s

weave. Figure 9 (a-d) illustrates that as the oil droplet's impact velocity v_O increases. The time to achieve maximum dilation decreases, while the maximum dilation D_{max} and anisotropic dilation ratio of the profiled surface increase.

Higher impact velocities increase the kinetic energy of the oil droplets, accelerating their spreading upon contact. The unique texture of the biomimetic surface introduces anisotropy, promoting rapid diffusion along specific microtexture paths. As the velocity increases, retraction is further accelerated, reducing the time to reach maximum diffusion. At higher impact velocities, oil droplets overcome greater surface resistance, enhancing diffusion. Unlike isotropic surfaces, anisotropic structures promote directional diffusion, particularly along horizontal axes parallel to the texture, resulting in larger diffusion diameters. This directional diffusion effect underscores the surface's ability to minimize interaction time and contact area with droplets, thereby enhancing oleophobic properties and facilitating droplet rebound.

Figure 10(a-d) illustrates the time-varying curves of the spreading diameter and spreading ratio of oil droplets impacting a surface with secondary bionic microstructures at varying velocities. Figure 10(a) show that the oil

droplets spread rapidly, reaching maximum diameters of 2.03 mm in the D_x -direction and 1.96 mm in the D_y -direction at 0.0125 s. Subsequently, the droplets underwent a process of shrinkage, ultimately resulting in a secondary rebound away from the surface of the primary weave. Figure 10(a-d) illustrates that as the oil droplet's impact velocity v_O increases. The time to reach maximum spreading diameter decreases, while the maximum diameter D_{max} increases gradually. Additionally, the anisotropic spreading ratio of the bionic surface appears to be significantly reduced. The time-varying curves are consistent with the time-varying curves of the first-grade bionic fabric.

As impact velocity increases, the higher kinetic energy accelerates initial diffusion and reduces the time required to reach maximum diffusion. The fine microtexture of the secondary biomimetic surface minimizes resistance, further promoting rapid diffusion. Consequently, higher velocities result in faster diffusion and a shorter time for the secondary biomimetic surface to reach its maximum diameter. As the impact velocity increases, the oil droplet's spreading diameter increases in proportion to its initial kinetic energy. The refined grooves of the secondary biomimetic surface effectively direct the
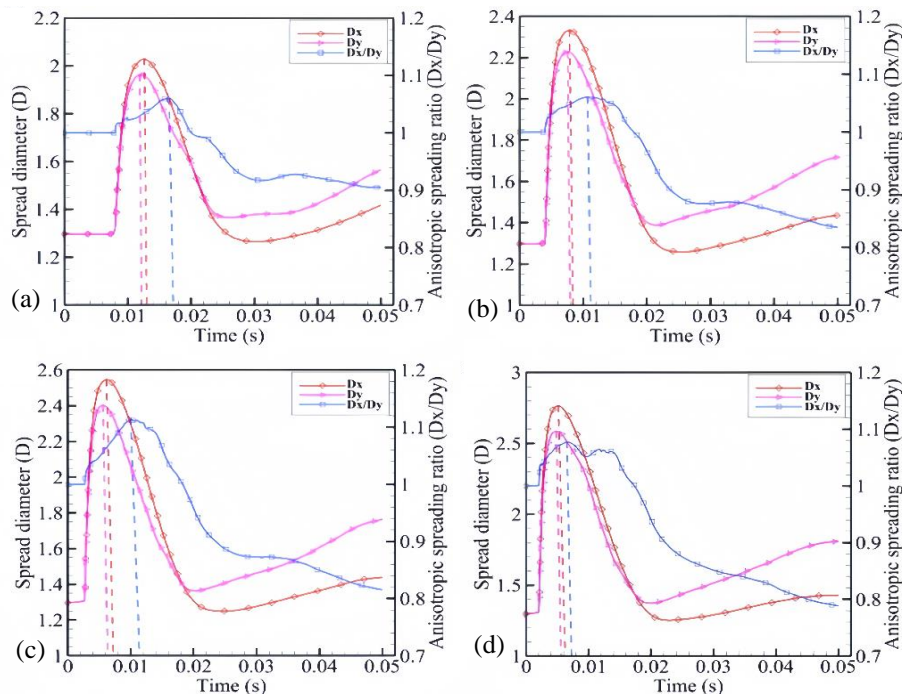
Fig. 10 Time-Varying Curves of Spreading Diameter and Anisotropic Spreading Ratio of Oil Droplets on Secondary Bionic Surfaces with Different Impact Velocities: (a) v_0 =0.5 m/s, (b) v_0 =1.0 m/s, (c) v_0 =1.5 m/s, (d) v_0 =2.0 m/s

oil outward, allowing it to spread further than on less textured surfaces. This structure also reduces oil droplet adhesion, which is reflected in its enhanced oleophobic properties, making the droplets more prone to rebound phenomena.

Analysis of oil droplet impacts on microtextured surfaces revealed significant differences in horizontal and vertical diffusion diameters on anisotropic biomimetic surfaces. As the impact velocity (v_0) of the oil droplet increases, the time required to reach the maximum spreading state in both horizontal and vertical directions gradually increases. Additionally, the horizontal spreading diameter exceeds the vertical one. The striping configuration facilitates horizontal spreading when the oil droplet extends parallel to the striping pattern, thereby prolonging the time required for the droplet to reach equilibrium. Consequently, the horizontal spreading diameter is greater than the vertical.

3.1.3 Comparative Evaluation of the Spreading Diameter Curves of Oil Droplets

This paper demonstrates significant differences in the distribution of oil droplets on smooth, primary biomimetic, and secondary biomimetic surfaces. The diffusion curves of oil droplets are compared, revealing that the maximum spreading diameter along the microweaving direction X exceeds that along direction Y. Consequently, the parallel microweaving direction is selected for further analysis. Figure 11(a-d) presents the time-varying curves of horizontal X spreading diameters for oil droplets at various impact velocities on smooth and primary bionic weave surfaces. The analysis shows that, with increasing velocity, oil droplets on both surfaces

reach their maximum spreading diameter more quickly, with higher velocities resulting in larger diameters. However, the smooth surface allows unrestricted diffusion of the oil droplets, leading to a larger diffusion diameter. In contrast, the primary bionic weave surface limits droplet diffusion due to its microtexture, which accelerates droplet retraction and enhances oleophobic properties. This structure restricts horizontal diffusion, reducing both interaction duration and diffusion diameter, particularly at higher velocities, suggesting improved sealing properties of the surface.

Figure 12(a-d) presents the time-varying curves of oil droplets at different impact velocities on primary and secondary bionic weave surfaces, aligned with the microarray structure X. The analysis indicates that, with increasing impact velocity, oil droplets on both primary and secondary bionic surfaces reach a larger maximum diffusion diameter more quickly. However, the finer microstructure of the secondary bionic surface more effectively restricts oil droplet spreading. Consequently, the maximum diameter of the droplets on the secondary bionic surface is smaller, and the interaction duration is shorter compared to the primary bionic surface. The fine structure of the secondary bionic surface enhances the air cushioning effect, reduces adhesion, and accelerates retraction and rebound. These factors highlight the superior sealing and oil-repellent properties of the secondary bionic surfaces.

The CFD method quantitatively analyzes droplet propagation on smooth and biomimetic surfaces at various velocities, revealing that the maximum propagation diameter on the latter is smaller. Secondary rebound on smooth surfaces remains unaffected by the impact
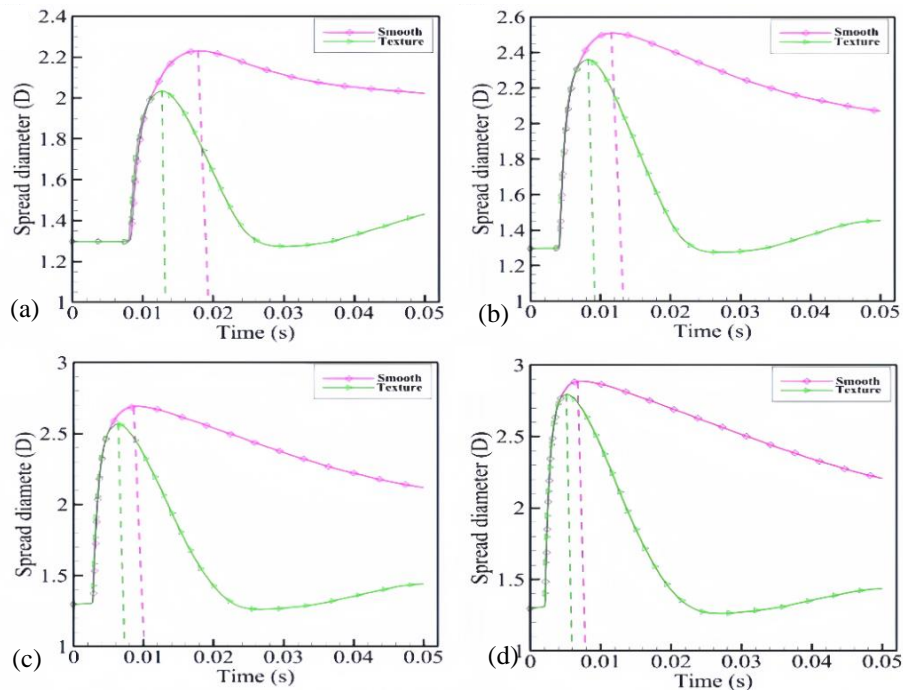
Fig. 11 Time-Varying Curves of Spreading Diameter of Oil Droplets with Different Impact Velocities on Smooth and Bionic Surfaces: (a) v_0 =0.5 m/s, (b) v_0 =1.0 m/s, (c) v_0 =1.5 m/s, (d) v_0 =2.0 m/s
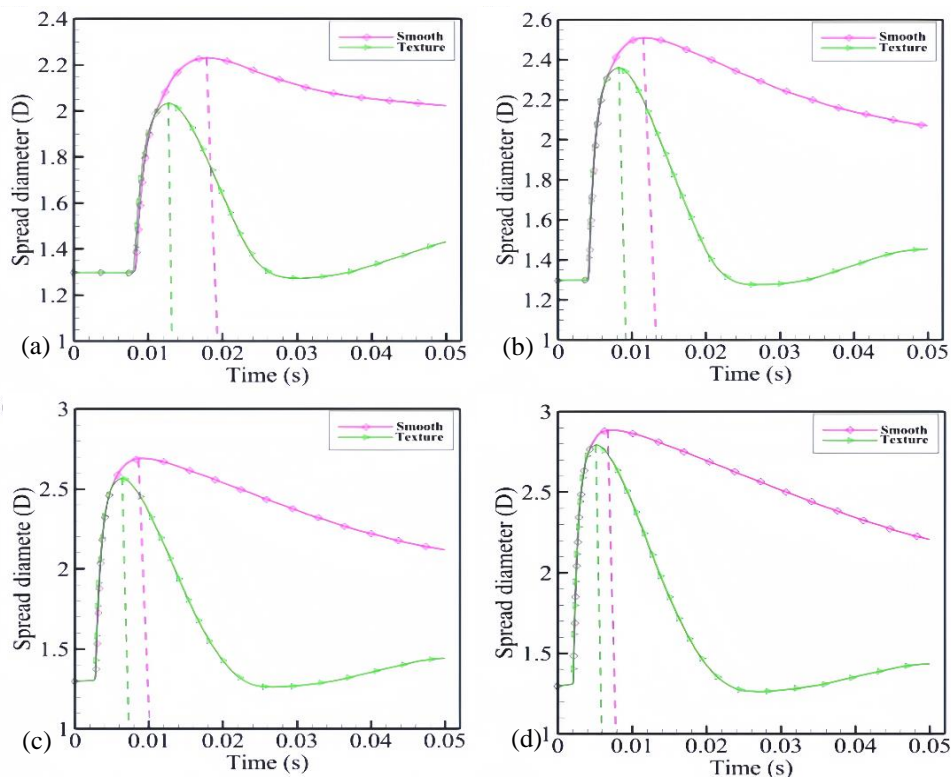
Fig. 12 Time-varying profiles of spreading diameters of oil droplets with different impact velocities on the surface of different bionic structures: (a) v_0 =0.5 m/s, (b) v_0 =1.0 m/s, (c) v_0 =1.5 m/s, (d) v_0 =2.0 m/s

velocity, showing no dependence on speed. However, for surfaces with parallel microarray patterns, the maximum spreading diameter of the droplets is noticeably larger in the parallel direction compared to the perpendicular direction. Therefore, the design and orientation of the

biomimetic structure have a direct impact on the droplets' dynamic spreading behavior. A superoleophobic biomimetic surface that features a grooved structure effectively limits the spreading of droplets in the perpendicular direction, while promoting greater expansion
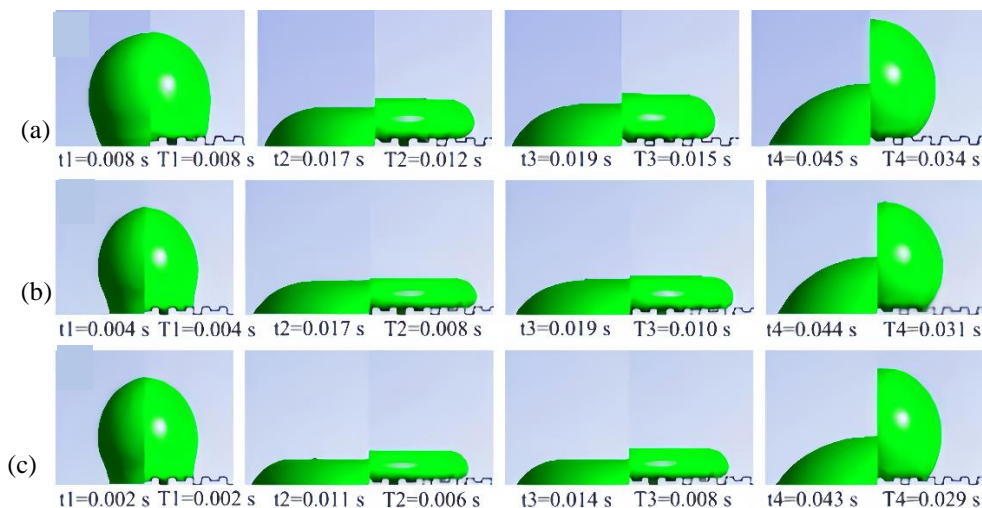
Fig. 13 Comparative analysis of the spreading state of oil droplets on smooth and bionic surfaces at varying impact velocities: (a) v_0 =0.5 m/s, (b) v_0 =1.0 m/s, (c) v_0 =1.5 m/s
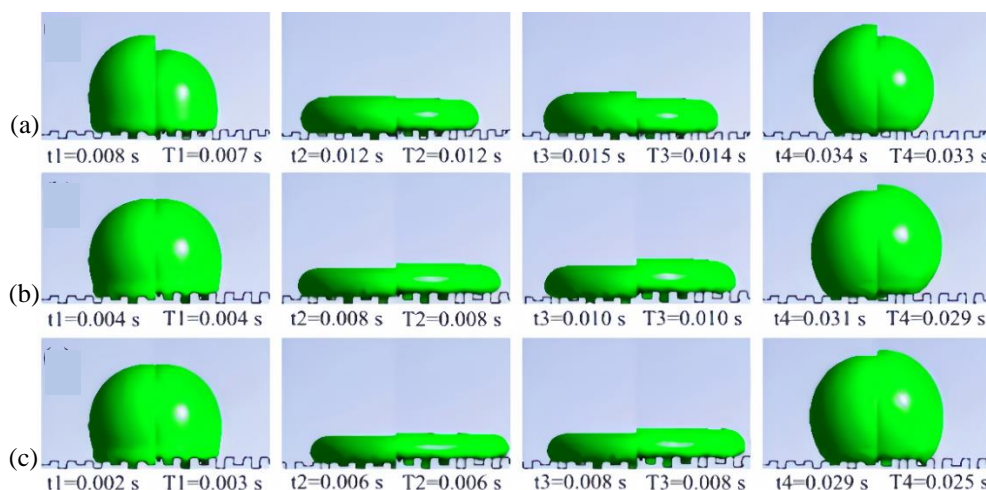
Fig. 14 Comparative analysis of the spreading state of oil droplets on primary and secondary bionic surfaces at different impact velocities: (a) v_0 =0.5 m/s, (b) v_0 =1.0 m/s, (c) v_0 =1.5 m/s

along the parallel axis. This arrangement also leads to a higher retraction rate when compared to a smooth surface, indicating the influence of structural orientation on droplet behavior.

3.2 Comparative Analysis of Oil Droplet Spreading State on Different Structured Surfaces

This study examines the dynamic behavior of biomimetic microarrays in droplet diffusion by analyzing the spreading behavior of oil droplets on different surface types. The spreading dynamics are evaluated qualitatively at three distinct impact velocities—0.5 m/s, 1.0 m/s, and 1.5 m/s—on both smooth and microtextured surfaces, as shown in Fig. 13(a-c). Time points t1 and T1 represent the moments when the oil droplets first make contact with the smooth and microtextured surfaces, respectively. At time points t2 and T2, the droplets reach their maximum spreading on these surfaces. Time points t3 and T3 mark the initiation of droplet desorption, and finally, at time points t4 and T4, the oil droplets are fully desorbed from the surfaces.

Our findings show that when an oil droplet contacts a smooth, lipophilic surface, it spreads and contracts but ultimately fails to fully desorb, remaining on the smooth surface. In contrast, oil droplets on the biomimetic superoleophobic surface with a microarray structure undergo a series of rapid changes. Initially, the droplets spread and contract rapidly, eventually detaching from the oleophobic surface in a fully contracted state. Upon impact with the non-smooth biomimetic superoleophobic surface at different velocities, the oil droplets achieve complete desorption. The time required for full desorption after the second bounce decreased from 0.034 s to 0.029 s as the droplet speed increased, representing a 14.7% reduction in desorption time.

Figure 14(a-c) illustrates the spreading behavior of oil droplets at varying impact velocities and times on primary and secondary biomimetic microtextured surfaces. It is evident that the oil droplets interact with two distinct microtextured surface structures. Both structures exhibit rapid spreading and contraction of the oil droplets, followed by rapid detachment from the oleophobic surface
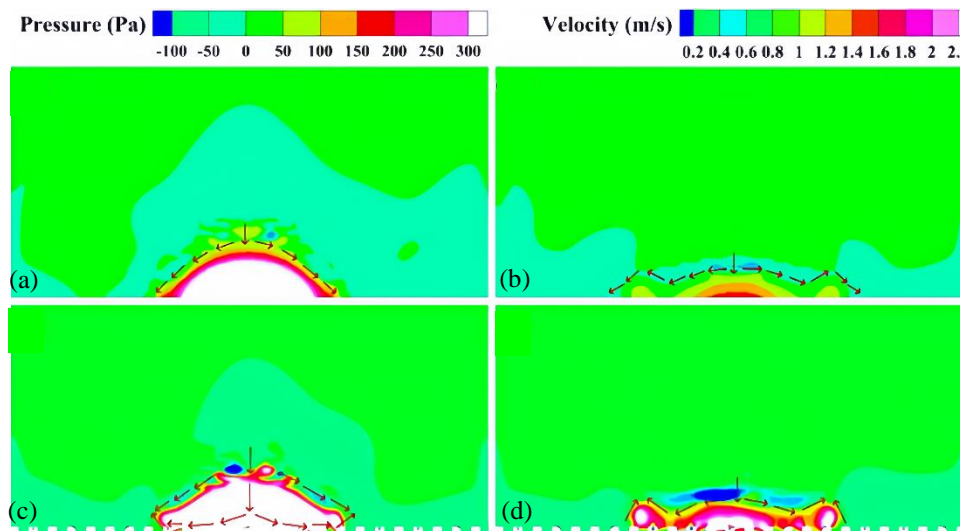
Fig. 15 Comparative analysis of pressure and velocity vector clouds during spreading and retraction of smooth and secondary bionic surfaces: (a) v_0 **=1.0 m/s, t=0.005 s; (b)** v_0 **= 1.0 m/s, t=0.006 s; (c)** v_0 **=1.0 m/s, t=0.004 s; (d)** v_0 **= 1.0 m/s, t=0.005 s**

in the fully contracted state. Compared to the primary structure, the secondary biomimetic weave surface, which features finer microweave units, enhances oleophobicity and promotes faster retraction. As a result, the maximum spreading diameter of the secondary surface is smaller, and it reaches this diameter more quickly than the primary surface. The study of the sealing properties of secondary biomimetic surfaces with smaller microweave units demonstrates superior performance compared to primary biomimetic weave surfaces.

Additionally, velocity and pressure vector field maps for smooth and secondary biomimetic surfaces during spreading and retraction at an impact velocity of 1.0 m/s were used to explain the spreading behavior, as shown in Fig. 15(a-d). During the spreading process, as depicted in Fig. 15(a) and (c), the smooth surface experiences a combination of gravity and interfacial resistance, leading to rapid spreading. In contrast, on secondary biomimetic weave surfaces, the low surface energy and high oleophobicity create air pockets upon droplet impact with the microarray structure. This phenomenon contributes to the observed rapid shrinkage before the droplet fully spreads. Furthermore, during retraction, as shown in Fig. 15(b) and (d), the adhesion force and gravity on the smooth surface dominate over surface tension and the droplet's retraction inertia, causing the oil droplet to spread out and become stationary on the surface. When an oil droplet impacts a secondary biomimetic surface, a contraction behavior similar to that of an eagle's wing is observed. This is due to the significant reduction in the reattachment phenomenon induced by the horizontal contraction of the oil droplet. The microarray structure contributes to an increased second bounce rate by enhancing the force exerted on the droplet, which minimizes its tendency to reattach. This effect reduces the interaction time between the oil droplet and the surface, slows down the droplet's spread, and significantly improves the sealing performance.

4. CONCLUSION

This study demonstrates that biomimetic superoleophobic surfaces, particularly those with secondary biomimetic microweave structures, can substantially enhance sealing performance, making them well-suited for applications requiring high oil resistance and minimal leakage, such as automotive engine gaskets. Through numerical simulations using CFD and VOF models, alongside experimental analysis, it was found that the biomimetic weaving surface effectively reduces the diffusion diameter of oil droplets and shortens the interaction time. Compared to smooth surfaces, the interaction duration was reduced by approximately 14.7%, and the diffusion diameter decreased by 15%. These results underscore the superior oleophobic properties of biomimetic structures.

The research also highlights the potential of incorporating advanced micrometer- and nanometer-scale structures into industrial seals to improve efficiency under extreme conditions. By fine-tuning the texture of the biomimetic surface through adjustments in weave pattern and size, significant improvements in durability and performance can be achieved. This approach offers a pathway for the development of innovative, high-performance, and sustainable sealing technologies.

CONFLICT OF INTEREST

The authors affirm that they have no financial or personal interests that could be perceived as influencing the outcomes or interpretation of this study.

AUTHORS CONTRIBUTION

Qinghua Li Providing the thinking of the study, the design of the procedure, and the analysis of the data. **Siyuan Cheng** Manuscript writing, graphing, and data collection. **Zhenhua Hou** Data collecting, analyzing, and researching documents. **Wanting Zhao** Data collection and study design. **Qingyu Guan** contributed by collecting data and performing the analysis. All authors have thoroughly reviewed and approved the final version of the manuscript for publication.

REFERENCES

Baggio, M., & Weigand, B. (2019). Numerical simulation of a drop impact on a superhydrophobic surface with a wire. *Physics of Fluids 31(11)*. http://doi.org/10.1063/1.5123593

Barthlott, W., Mail, M., Bhushan, B., & Koch, K. (2017). Plant surfaces: structures and functions for biomimetic innovations. *Nano-Micro Letters, 9*, 1-40. http://doi.org/10.1007/s40820-016-0125-1

Chila, R. J., & Kaminski, D. A. (2008). Grid Independence via automated unstructured adaptation. *of Fluids Engineering,* 121403. http://doi.org/10.1115/1.3001099

Ding, W., Fernandino, M., & Dorao, C. A. (2019). Conical micro-structures as a route for achieving super-repellency in surfaces with intrinsic hydrophobic properties. *Applied Physics Letters, 115(5)*. http://doi.org/10.1063/1.5096776

Dodson, R. F., & Hammar, S. P. (2005). *Asbestos: risk assessment, epidemiology, and health effects. CRC Press*. https://doi.org/10.1201/9781420038149

Dong, L., Li, K., Zhu, X., Li, Z., Zhang, D., Pan, Y., & Chen, X. (2020). Study on high temperature sealing behavior of packer rubber tube based on thermal aging experiments. *Engineering Failure Analysis, 108*, 104321. http://doi.org/10.1016/j.engfailanal.2019.104321

Farfán-Cabrera, L. I., Pérez-González, J., & Gallardo-Hernández, E. A. (2018). Deterioration of seals of automotive fuel systems upon exposure to straight Jatropha oil and diesel. *Renewable Energy*, *127*, 125-133. https://doi.org/10.1016/j.renene.2018.04.048

Feng, L., Zhang, Y., Xi, J., Zhu, Y., Wang, N., Xia, F., & Jiang, L. (2008). Petal effect: a superhydrophobic state with high adhesive force. *Langmuir*, *24(8)*, 4114-4119. http://doi.org/10.1021/la703821h

Gao, S. R., Jin, J. X., Wei, B. J., Lin, D. J., Wang, X., Zhang, L. Z., Yang, Y. R., & Wang, X. D. (2021). Dynamic behaviors of two droplets impacting an inclined superhydrophobic substrate. *Colloids and Surfaces A: Physicochemical and Engineering Aspects,* *623*, 126725. http://doi.org/10.1016/J.COLSURFA.2021.126725

Gauthier, A., Symon, S., Clanet, C., & Quéré, D. (2015). Water impacting on superhydrophobic macrotextures. *Nature Communications, 6(1)*, 8001. http://doi.org/10.1038/ncomms9001

Gose, J. W., Golovin, K., Boban, M., Mabry, J. M., Tuteja, A., Perlin, M., & Ceccio, S. L. (2018). Characterization of superhydrophobic surfaces for drag reduction in turbulent flow. *Journal of Fluid Mechanics*, *845*, 560-580. http://doi.org/10.1017/jfm.2018.210

Guo, Z., & Liu, W. (2007). Biomimic from the superhydrophobic plant leaves in nature: Binary structure and unitary structure. *Plant Science, 172*, 1103-1112. http://doi.org/10.1016/j.plantsci.2007.03.005

Huang, Q., Zhang, Y., & Pan, G. (2016). Dynamic behaviors and energy transition mechanism of droplets impacting on hydrophobic surfaces. *Discrete Dynamics in Nature and Society, 2016*, 1-9. https://doi.org/10.1155/2016/8517309

Jia, W., Li, M., Weng, H., Gu, G., & Chen, Z. (2020). Design and comprehensive assessment of a biomimetic tri-layer tubular scaffold via biodegradable polymers for vascular tissue engineering applications. *Materials Science and Engineering: C, 110*, 110717. http://doi.org/10.1016/j.msec.2020.110717

Jiang, S., Guo, Z., Gyimah, G. K., Zhang, C., & Liu, G. (2018). Preparation of biomimetic superhydrophobic surface by a facile one-step pulse electrodeposition. *Procedia CIRP, 68*, 237-241. http://doi.org/10.1016/j.procir.2017.12.055

Li, J., Yang, K., Liang, Y., & Liu, C. (2022). Hydrodynamic analysis of the energy dissipation of droplets on vibrating superhydrophobic surfaces. *International Journal of Heat and Mass Transfer*, *137*, 106264. https://doi.org/10.1016/j.icheatmasstransfer.2022.106264

Li, Z., Hu, R., Song, J., Liu, L., Qu, J., Song, W., Cao, C. (2021). Gas–liquid–solid triphase interfacial chemical reactions associated with gas wettability. *Advanced Materials Interfaces*, *8(6)*, 2001636. http://doi.org/10.1002/ADMI.202001636

Liang, Y. H., Peng, J., Li, X. J., Xu, J. K., Zhang, Z. H., & Ren, L. Q. (2016). From natural to biomimetic: The superhydrophobicity and the contact time. *Microscopy Research and Technique*, *79(8)*, 712-720. http://doi.org/10.1002/jemt.22689

Lin, D. J., Zhang, L. Z., Yi, M. C., Wang, X., Gao, S. R., Yang, Y. R., Zheng, S. F., & Wang, X. D. (2020). Contact time of double-droplet impacting superhydrophobic surfaces with different

macrotextures. *Processes, 8(8)*, 896. http://doi.org/10.3390/pr8080896

Liu, C., Liu, Q., & Lin, Z. (2020). Dynamical behavior of droplets transiently impacting on superhydrophobic microstructures. *Physics of Fluids, 32(10)*. http://doi.org/10.1063/5.0024400

Luo, W., Yu, B., Xiao, D., Zhang, M., Wu, X., & Li, G. (2018). Biomimetic superhydrophobic hollowed-out pyramid surface based on self-assembly. *Mater, 11(5)*, 813. http://doi.org/10.3390/ma11050813

Marengo, M., Antonini, C., Roisman, I. V., & Tropea, C. (2011). Drop collisions with simple and complex surfaces. *Current Opinion in Colloid & Interface Science, 16(4)*, 292-302. http://doi.org/10.1016/j.cocis.2011.06.009

Nagashima, T., & Sawada, M. (2016). Development of a damage propagation analysis system based on level set XFEM using the cohesive zone model. *Computers & Structures, 174*, 42-53. http://doi.org/10.1016/j.compstruc.2015.10.005

Nekouei, M., & Vanapalli, S. A. (2017). Volume-of-fluid simulations in microfluidic T-junction devices: Influence of viscosity ratio on droplet size. *Physics of Fluids, 29(3)*. http://doi.org/10.1063/1.4978801

Serevina, V., & Meyputri, C. U. (2021, September.3–4). *Development of blended learning based on website on fluid mechanic material to improve students' creative thinking skills*. IOP Publishing 2020, Journal of Physics: Conference Series. http://doi.org/10.1088/1742-6596/1876/1/012070

Talebanfard, N., Nemati, H., & Boersma, B. J. (2019). Heat transfer in deforming droplets with a direct solver for a coupled level-set and volume of fluid method. *International Communications in Heat and Mass Transfer, 108*, 104272. http://doi.org/10.1016/j.icheatmasstransfer.2019.104272

Vander Veen, R. C. A., Hendrix, M. H. W., Tran, T., Sun, C., Tsai, P. A., & Lohse, D. (2014). How microstructures affect air film dynamics prior to drop impact. *Soft Matter, 10(21)*, 3703-3707. http://doi.org/10.1039/c4sm00298a

Walters, D. K., & Wolgemuth, N. M. (2009). A new interface-capturing discretization scheme for numerical solution of the volume fraction equation in two–phase flows. *International Journal for Numerical Methods in Fluids, 60(8)*, 893-918. http://doi.org/10.1002/fld.1924

Wang, G., Liang, W., Wang, B., Zhang, Y., Li, J., Shi, L., & Guo, Z. (2013). Conductive and transparent superhydrophobic films on various substrates by in situ deposition. *Applied Physics Letters, 102(20)*. http://doi.org/10.1063/1.4807472

Wang, B., Liang, W., Guo, Z., & Liu, W. (2015). Biomimetic super-lyophobic and super-lyophilic materials applied for oil/water separation: a new strategy beyond nature. *Chem. Soc. Rev, 44(1)*, 336-361. http://doi.org/10.1039/c4cs00220b

Wang, Y., Wang, Q., Wang, B., Tian, Y., Di, J., Wang, Z., Jiang, L., & Yu, J. (2021). Modulation of solid surface with desirable under-liquid wettability based on molecular hydrophilic–lipophilic balance. *Chemical Science, 12(17)*, 6136-6142. https://doi.org/10.1039/d1sc00808k

Wu, J., Ma, R., Wang, Z., & Yao, S. (2011). Do droplets always move following the wettability gradient? *Applied Physics Letters 98(20)*. https://doi.org/10.1063/1.3592997

Wu, L., Gong, M., & Wang, J. (2018). Development of a DEM–VOF model for the turbulent free-surface flows with particles and its application to stirred mixing system. *Industrial & Engineering Chemistry Research, 57(5)*, 1714-1725. http://doi.org/10.1021/acs.iecr.7b04833

Yarin, A. L. (2006). Drop impact dynamics: Splashing, spreading, receding, bouncing. *Annual Review of Fluid Mechanics, 38*, 159-192. https://doi.org/10.1146/annurev.fluid.38.050304.092144

Zhang, G. L., Zhang, W. J., Li, H. L., Cao, W. Z., Wang, B. D., Guo, W. S., & Guo, P. (2021). Waterproofing behavior of sealing gaskets for circumferential joints in shield tunnels: A full-scale experimental investigation. *Tunnelling and Underground Space Technology, 108*, 103682. http://doi.org/10.1016/j.tust.2020.103682

Zhang, J., & Hu, Y. (2020). Sealing performance and mechanical behavior of PEMFCs sealing system based on thermodynamic coupling. *International Journal of Hydrogen Energy, 45(43)*, 23480–23489. https://doi.org/10.1016/j.ijhydene.2020.06.167

Zhang, X., Liu, X., Wu, X., & Min, J. (2020). Impacting-freezing dynamics of a supercooled water droplet on a cold surface: Rebound and adhesion. *International Journal of Heat and Mass Transfer, 158*, 119997. http://doi.org/10.1016/j.ijheatmasstransfer.2020.119997

Zhao, C., Montazeri, K., Shao, B., & Won, Y. (2021). Mapping between surface wettability, droplets, and their impacting behaviors. *Langmuir, 37(33)*, 9964-9972. http://doi.org/10.1021/acs.langmuir.1c00879